GEOPHYSICS, VOL. 81, NO. 1 (JANUARY-FEBRUARY 2016); P. V1–V6, 3 FIGS.
10.1190/GEO2015-0117.1

Wave-equation-based image warping

Adel Khalil[1] and Henning Hoeber[1]

ABSTRACT

In seismic processing and reservoir characterization, we often need to measure relative displacements between different realizations of data. Over the years, many methods have been developed using different measures of similarity. Such alignment or warping methods are often effective signal or image processing tools. However, none of the available methods are directly driven by the physics of seismic imaging. We have found that a seismic image can be considered as a field governed by the wave equation. We visualized different image realizations as snapshots of the wavefield at different times, and these conveyed the required displacements or time shifts. By formulating the problem in a physical context, we obtained displacements that honored the directionality of the wave propagation. For example, 4D time shifts on migrated stacks were obtained in a direction normal to the reflectors. We have computed these shifts in an inverted finite-difference scheme. To overcome limitations of the two-way wave equation in this application, we factorized it to its one-way counterparts. The method was demonstrated on synthetic and real data sets.

INTRODUCTION

Throughout the seismic processing sequence, and for reservoir analysis, relative shifts between different data sets are frequently needed. These shifts can be calculated preimaging, for example, to reduce the acquisition footprint, or postimaging, for example, to derive trim statics (Gulunay et al., 2007). Measuring relative displacements between different data realizations is particularly important in time-lapse processing in which time shifts may highlight production-related changes within the reservoir (Williamson et al., 2007). Over the years, many methods have been developed, often using local crosscorrelations or other similarity-based methods (e.g., Hall, 2006; Hale, 2009, 2013; Baek et al., 2014). In its different forms, warping is a useful tool to estimate these relative displacements.

Although warping is often an effective image processing technique, it is not directly driven by the physics of seismic imaging. The resulting displacement fields may not be unique, and inverting for geologically induced changes can be difficult. We show that a seismic image can be considered as a wavefield following a governing wave equation. Different image realizations, for example, base and monitor data sets, are visualized as snapshots of a wavefield at different time steps. These spatially varying time shifts are then computed in an inverted finite-difference scheme in which the wavefield is fully known, but the step value is not.

To estimate the wavefield at a given time, the two-way wave equation requires at least the knowledge of the wavefield at the two preceding time steps. This is not readily available in an image warping context. We solve this issue by factorizing the two-way wave equation into its one-way counterparts.

THEORY

Reverse time migration (RTM) (Baysal et al., 1983; McMechan, 1983; Whitmore, 1983) is an indispensable imaging tool, particularly in complex geologies. One limitation of RTM is that producing angle gathers is not straightforward. Sava and Fomel (2006) derive a relationship that couples reflection angle to temporal frequency, image wavenumber, and the medium velocity:

$$\frac{4\cos^2(\theta)}{c^2(\underline{x})}\omega^2 = |\underline{k}|^2, \tag{1}$$

where $\underline{x} = (x, y, z)$ is the space coordinate vector, $c(\underline{x})$ is the velocity of the medium, θ is the reflection angle between the source and the receiver wavefields, ω is the angular frequency, and $\underline{k} = (k_x, k_y, k_z)$ is the wavenumber vector of the imaged data.

Equation 1 is derived using a purely geometric consideration of source and receiver wavefields, and it is applicable in many contexts different from RTM angle gather generation, for example, it is used to remove RTM low-frequency artifacts (Zhang and Sun, 2009).

Manuscript received by the Editor 25 February 2015; revised manuscript received 6 July 2015; published online 8 October 2015.
[1]CGG Services UK Limited, Research and Development, Aberdeen, UK. E-mail: adel.khalil@cgg.com; henning.hoeber@.cgg.com.

This relationship also holds for other migration methods, such as the Kirchhoff (Schneider, 1978; Gray and May, 1994) and Beam (Hill, 2001) methods. The theory of wavenumber scattering within the Born approximation is discussed by Wu and Toksoz (1987).

If equation 1 is considered in a domain in which the reflection angle is stationary, i.e., a common reflection angle section, the relationship readily translates into a dispersion relation for a new wave equation:

$$\frac{1}{v_\theta^2(\underline{x})}\partial_t^2 p_\theta(\underline{x};t) = \nabla^2 p_\theta(\underline{x};t), \tag{2}$$

where t is the time coordinate, p_θ represents the wavefield of the seismic image at one reflection angle, ∇^2 is the Laplacian operator, and $v_\theta(\underline{x})$ is given by

$$v_\theta(\underline{x}) = \frac{1}{2}\frac{c(\underline{x})}{\cos(\theta)}. \tag{3}$$

Equation 2 demonstrates that a seismic image from a constant angle section is the solution of a wave equation, in which the "velocity" is half that of the original medium velocity divided by the cosine of the reflection angle. The half factor is associated with the use of two-way time, whereas the cosine factor represents the migration stretch. An alternative heuristic derivation of equation 2 using the crosscorrelation imaging condition is given in Appendix A. The concept of viewing seismic images as wavefields has been explored before in Hubral et al. (1996) in what they call *seismic image waves*. Mosher et al. (1996) also derive a relationship similar to equation 2 in their common-angle time migration scheme.

Equation 2 is second order with respect to time; the solution requires the knowledge of the initial state of the wavefield and its temporal derivative. This information is generally not readily available within the context of image warping. This practically manifests itself as the inability of the equation to discriminate between positive and negative shifts without external information. To overcome this issue, we factorize equation 2 to its one-way counterparts. We follow the technique used to derive the Dirac equation (Dirac, 1928). To simplify the notation, we drop the spatial, temporal, and angle dependency:

$$\frac{1}{v}\partial_t \mathbf{p} = \pm\boldsymbol{\sigma}.\nabla\mathbf{p}, \tag{4}$$

where $\boldsymbol{\sigma}$ is the Pauli vector and $\boldsymbol{\sigma}.\nabla$ is the square root of the Laplacian operator, i.e., the Dirac operator. The derivation of equation 4 and the structure of the Pauli vector and matrices are given in Appendix B.

The bold notation of the image wavefield $\mathbf{p}$ in equation 4 denotes that it is now considered as a dual-component complex vector in a quantum mechanical context defined as a *spinor*. To relate the observed image wavefield to the spinor space, the wavefield is projected onto the eigenspace of the Dirac operator:

$$\mathbf{p} = \mathbf{K}[p], \tag{5}$$

where $\mathbf{K}$ is the eigenspace projection operator; this operator and the eigenvectors are defined in Appendix C.

Equation 4 is first order in time, and a simple finite-difference discretization scheme may be defined as

$$\frac{1}{v}\frac{\delta\mathbf{p}}{\Delta t} = \pm\boldsymbol{\sigma}.\nabla\mathbf{p}, \tag{6}$$

and

$$\delta\mathbf{p} = \mathbf{p}_{\pm\Delta t} - \mathbf{p}, \tag{7}$$

where $\mathbf{p}_{\pm\Delta t}$ is the image wavefield propagated for a duration of $\pm\Delta t$. The choice of sign is arbitrary, and is only a matter of convenience.

In the context of image warping, we are interested in finding the spatially variable time shift Δt rather than the propagating wavefields. To compute the time shift, we rearrange equation 6 and find the least-squares solution:

$$\Delta t = \frac{1}{v}\Re\left[\frac{\pm(\boldsymbol{\sigma}.\nabla\mathbf{p})^H(\delta\mathbf{p})}{(\boldsymbol{\sigma}.\nabla\mathbf{p})^H(\sigma.\nabla\mathbf{p}) + \varepsilon^2}\right], \tag{8}$$

where ε^2 is white noise to avoid divisions by zero, $\Re$ extracts the real component of the solution, and the superscript H denotes the Hermitian conjugate. Note that the time shift is spatially varying: $\Delta t = \Delta t(\underline{x})$.

To estimate the time shift between two data sets, we inject the two images into $\mathbf{p}$ and $\mathbf{p}_{\pm\Delta t}$ using equation 5. The two injected data sets may represent angle stacks for trim-statics estimation leading to improved focusing, or in a time-lapse context, the data sets may be base and monitor images leading to a 4D time-shift volume. The extracted shifts are in the direction normal to the wavefield, which better represents reservoir-related changes (Thore et al., 2012). In theory, the technique should be applied on common reflection-angle volumes. In practice, the migrated stacks can be used directly because they are often assumed to have a zero reflection angle.

Normally, time shifts required in seismic processing are scalar quantities, and their direction is not required; however, the Dirac-based wavefield decomposition presented in this article allows us to determine the propagation direction of a wavefield. In the context of image warping, these are the dips of imaged reflectors. This is given by the vector $\underline{u} = (u_x, u_y, u_z)$ defined in Appendix B.

EXAMPLES

Computing 3D displacement shifts for dipping reflectors

First, we demonstrate the method with a simple synthetic data set. The image is composed of four dipping reflectors. Two realizations are generated, with positive and negative 5-m displacements in the vertical direction. The normal displacement is the vertical displacement multiplied by the cosine of the dip angle. Figure 1 shows the resulting displacement shifts and their application. The normal shifts are correctly estimated by the method, and they completely remove the difference energy when applied to the input data sets. The orientation of the shifts is also calculated and demonstrated by the solid black lines in Figure 1c.

A real time-lapse data set from the North Sea

In this example, we demonstrate the method on two vintages from a North Sea data set. The structure is complex and contains steeply dipping flanks of a salt body. Figure 2 shows the two data

sets, and the 4D difference sections before and after the relative time shifts are applied. The 4D difference section after applying the shifts is cleaner confirming that the process is correctly estimating the relative shifts. Figure 3 shows these estimated time shifts with the 4D difference overlaid on the top. The correlation between the shifts and the difference energy is observed. The shifts are also oriented toward the direction of the seismic reflectors as expected.

NUMERICAL IMPLEMENTATION

Naïve implementation of the proposed method may lead to unstable or inaccurate results. At its heart, the method is a finite-difference scheme that inherits all the limitations of discretized approximations of the wave equation. Stability criteria such as the Courant-Friedrichs-Lewy criterion and numerical dispersion effects have to be considered. Robertsson et al. (2012) provide an extensive list of references on the accuracy and stability of finite-difference methods. These issues may appear as cycle skipping. A multiscale strategy similar to Bunks et al. (1995) helps in avoiding most of these difficulties. Lower wavenumbers are addressed first, then gradually moving onto higher scales.

Most warping methods based on the energy minimization are not necessarily symmetric with respect to the two data sets being processed. Depending on which data set is being used as a reference, the estimated time shifts vary. The presented method is no exception. The nonsymmetric nature arises due to the noise in the images and genuine amplitude differences. Constraining the least-squares problem to enforce reciprocity overcomes these effects.

DISCUSSION

Throughout this article, we discuss relative shift estimation between data sets using an inverted finite-difference approach. In this strategy, both data sets are viewed as snapshots of the same image wavefield. Alternatively, each image wavefield can be propagated independently and time shifts between different image realizations are extracted along the newly formed time axis. Each strategy has its merits; although the inverted finite-difference scheme is efficient, the independent propagation approach enables the use of traditional well-established 1D methods. Concepts such as time-strain (temporal derivative of the time shifts) inversion are easily applicable.

In practice, the migrated stacks can be used directly in the presented framework because they are often assumed to have a zero reflection angle. When the method is used on prestack data, for example, to compute residual moveout on common-angle gathers for a tomographic update, the shifts from each angle stack are altered according to the angle-dependent propagation velocity. This ensures that the angle volumes are treated properly, taking into account the migration stretch and

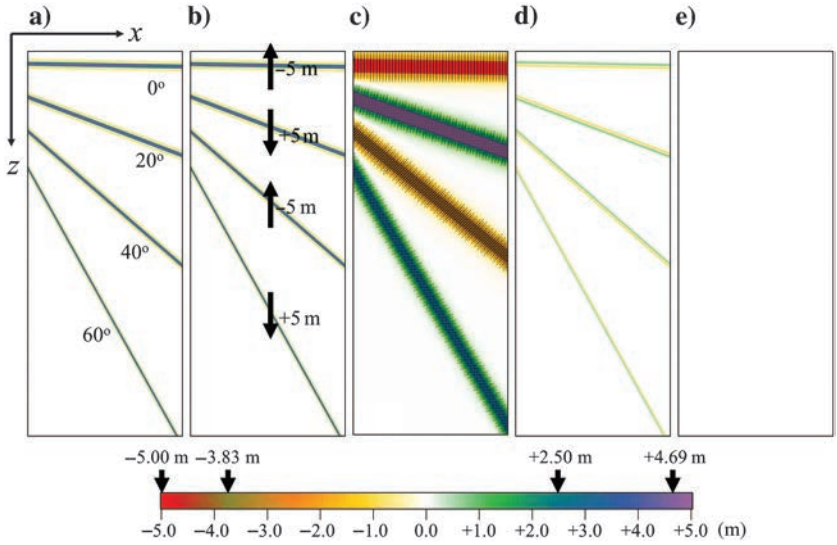

Figure 1. A synthetic data set composed of four dipping layers. (a) The base data set. (b) The monitor data set, generated by applying positive and negative 5-m shifts in the vertical direction. (c) The estimated normal displacements: These correctly match theoretical values (±5 m) cos (dip angle) and the solid black lines show their orientation. (d) The difference between panels (a and b). (e) The difference after applying the estimated shifts to panel (b).

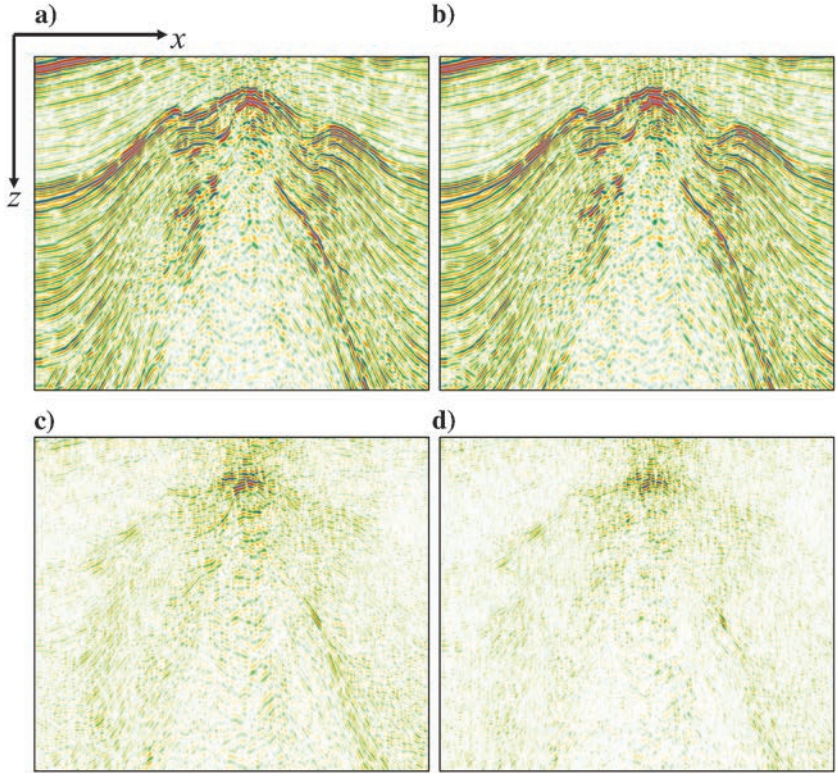

Figure 2. A real data set from the North Sea: (a) the base data set, (b) the monitor data set, (c) the 4D difference section between the base and monitor data sets, and (d) the 4D difference section after applying the estimated shifts.

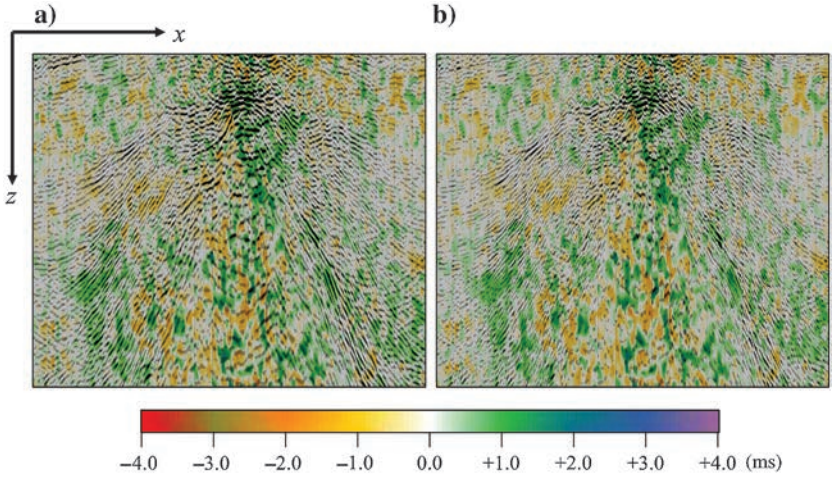

Figure 3. The 4D difference section overlaid on the top of the estimated time shifts. (a) Before applying the shifts and (b) after applying the shifts.

the fact that the time shift depends on the scattering angle. One shortcoming of the method is that it does not incorporate anisotropy.

CONCLUSIONS

We have developed a new approach to image warping that is based on the physics of seismic imaging. By formulating the problem in the context of wavefield propagation, displacements are obtained normal to the wavefronts unlike in conventional techniques, such as 1D warping. Effectively, the method acts as a wavefield-driven refocusing operation on seismic images; therefore, it is favorable in terms of preserving the true characteristics of the data, such as spectral content and amplitude. The effectiveness is demonstrated on real and synthetic data sets.

The concept of visualizing the seismic image as a wavefield is applicable to other domains, for example, in a velocity model update setting. Factorization of the wave equation has other potential applications, for example, in RTM imaging and 3D angle gather generation.

ACKNOWLEDGMENTS

We thank CGG for permitting to publish this work and BP for allowing us to show the real data example. Great appreciation is owed to C. Dervish-Uman, B. Deschizeaux, S. Gray, F. Perrone, J. Sun, Y. Zhang, and BP's North Sea seismic delivery team for constructive discussions and support.

APPENDIX A

DERIVATION OF THE ANGLE-DOMAIN IMAGE WAVE EQUATION

In seismic migration, the image is formed by propagating source and receiver wavefields and then applying the imaging condition. Commonly, the crosscorrelation imaging condition is used as follows:

$$p_I(\underline{x};\omega) = p_S(\underline{x};\omega)p_R^H(\underline{x};\omega), \tag{A-1}$$

where p_I, p_S, and p_R are the image, source, and receiver wavefields, respectively.

Applying the Laplacian to both sides of equation A-1 provides the following equation:

$$\nabla^2 p_I = p_S\nabla^2 p_R^H + p_R^H\nabla^2 p_S + 2\nabla p_S.\nabla p_R^H. \tag{A-2}$$

The source and receiver wavefields satisfy the wave equation; that is,

$$\frac{-\omega^2}{c^2}p_S = \nabla^2 p_S, \qquad \frac{-\omega^2}{c^2}p_R = \nabla^2 p_R. \tag{A-3}$$

Substituting equation A-3 into A-2 gives

$$\nabla^2 p_I = -2\frac{\omega^2}{c^2}p_S p_R^H + 2\nabla p_S.\nabla p_R^H. \tag{A-4}$$

Now, we define the quantity $\cos(2\theta)$ as follows:

$$\cos(2\theta) \equiv \frac{c^2\nabla p_S.\nabla p_R^H}{-\omega^2 p_S p_R^H}. \tag{A-5}$$

Substituting equations A-1 and A-5 into equation A-4, we have

$$\nabla^2 p_I = -2\frac{\omega^2}{c^2}p_I - 2\frac{\omega^2}{c^2}\cos(2\theta)p_I. \tag{A-6}$$

Expanding equation A-6 using the double-angle rule gives

$$\nabla^2 p_I = -4\frac{\omega^2}{c^2}\cos^2(\theta)p_I. \tag{A-7}$$

Equation A-7 can then be written as

$$\nabla^2 p_I = \frac{1}{v_\theta^2}\partial_t^2 p_I, \qquad v_\theta = \frac{1}{2}\frac{c}{\cos(\theta)}. \tag{A-8}$$

Equation A-8 shows that the image is a solution of a wave equation. Now, we need to verify that θ in relationship A-5 indeed represents the reflection angle.

The source and receiver wavefields can be viewed as a superposition of plane waves; that is,

$$p_S(\underline{x};\omega) = \int P_S(\underline{k}_S;\omega)e^{+i\underline{k}_S.\underline{x}}d\underline{k}_S,$$
$$p_R(\underline{x};\omega) = \int P_R(\underline{k}_R;\omega)e^{+i\underline{k}_R.\underline{x}}d\underline{k}_R, \tag{A-9}$$

where $\underline{k}_S$ and $\underline{k}_R$ are the source and receiver wavenumber vectors, respectively.

Substituting equation A-9 into equation A-5, we have

$$\cos(2\theta) = \frac{\int i\underline{k}_S \cdot i\underline{k}_R P_S P_R^H e^{+i\underline{k}_S\cdot\underline{x}-i\underline{k}_R\cdot\underline{x}} d\underline{k}_S d\underline{k}_R}{\left(\int \frac{i\omega}{c} P_S e^{+i\underline{k}_S\cdot\underline{x}} d\underline{k}_S\right)\left(\int \frac{i\omega}{c} P_R^H e^{-i\underline{k}_R\cdot\underline{x}} d\underline{k}_R\right)}. \tag{A-10}$$

Note that the integration is performed only over the region defined by $\underline{k} = \underline{k}_S + \underline{k}_R$, where $\underline{k}$ is the image wavenumber vector. The source and receiver wavefields satisfy the wave equation and its dispersion relation; therefore, equation A-10 can be written as

$$\cos(2\theta) = \frac{\int \underline{k}_S.\underline{k}_R P_S P_R^H e^{+i\underline{k}_S\cdot\underline{x}-i\underline{k}_R\cdot\underline{x}} d\underline{k}_S d\underline{k}_R}{\int |\underline{k}_S||\underline{k}_R| P_S P_R^H e^{+i\underline{k}_S\cdot\underline{x}-i\underline{k}_R\cdot\underline{x}} d\underline{k}_S d\underline{k}_R}. \tag{A-11}$$

For any given source and receiver wavenumber vectors, the integrals are dropped, and the equation readily translates to the famous dot product rule for calculating the angle between two vectors

$$\cos(2\theta) = \frac{\underline{k}_S.\underline{k}_R}{|\underline{k}_S||\underline{k}_R|}. \tag{A-12}$$

Equation A-12 shows that indeed θ in relationship A-5 corresponds to the reflection angle.

APPENDIX B

THE FACTORIZED WAVE EQUATION AND PAULI MATRICES

The acoustic source-free two-way wave equation is given by

$$\left(\frac{1}{c^2(\underline{x})}\partial_t^2 - \nabla^2\right) p = 0. \tag{B-1}$$

To factorize this wave equation into its one-way counterpart, we seek an equation of the form

$$\left(\frac{1}{c(\underline{x})}\partial_t - \sqrt{\nabla^2}\right)\left(\frac{1}{c(\underline{x})}\partial_t + \sqrt{\nabla^2}\right) p = \Gamma p, \tag{B-2}$$

where Γ is some form of the reflectivity operator and $\sqrt{\nabla^2}$ is the square root of the Laplacian operator that satisfies the relation

$$\sqrt{\nabla^2}\sqrt{\nabla^2} p = \nabla^2 p. \tag{B-3}$$

An explicit form of the $\sqrt{\nabla^2}$ operator cannot be defined for scalar fields; however, if p is defined as a dual-component complex vector $\mathbf{p}$, i.e., a spinor, the Dirac operator may take the form

$$\boldsymbol{\sigma}.\nabla = \boldsymbol{\sigma}_x\partial_x + \boldsymbol{\sigma}_y\partial_y + \boldsymbol{\sigma}_z\partial_z, \tag{B-4}$$

where the Pauli matrices defining this operator are given by

$$\boldsymbol{\sigma}_x = \begin{pmatrix} 0 & 1 \\ 1 & 0 \end{pmatrix}, \quad \boldsymbol{\sigma}_y = \begin{pmatrix} 0 & -i \\ i & 0 \end{pmatrix}, \quad \boldsymbol{\sigma}_z = \begin{pmatrix} 1 & 0 \\ 0 & -1 \end{pmatrix}. \tag{B-5}$$

The key properties allowing this formulation are the relations

$$\boldsymbol{\sigma}_i\boldsymbol{\sigma}_i = \mathbf{I}, \qquad \boldsymbol{\sigma}_i\boldsymbol{\sigma}_j = -\boldsymbol{\sigma}_j\boldsymbol{\sigma}_i, \tag{B-6}$$

where subscripts i and j denote any of the three space coordinates. Using these properties, it is easily verifiable that the Dirac operator is the square root of the Laplacian operator; that is,

$$(\boldsymbol{\sigma}.\nabla)(\boldsymbol{\sigma}.\nabla)\mathbf{p} = \nabla^2\mathbf{p}. \tag{B-7}$$

Rewriting equation B-2 in terms of the Dirac operator leads to

$$\left(\frac{1}{c(\underline{x})}\partial_t - \sigma.\nabla\right)\left(\frac{1}{c(\underline{x})}\partial_t + \sigma.\nabla\right)\mathbf{p} = -\left(\sigma\cdot\frac{\nabla c}{c}\right)\frac{1}{c}\partial_t\mathbf{p}. \tag{B-8}$$

The coupling term on the right side of the equation is a function of the velocity gradient, and it is interpreted as a reflectivity operator. Because we are not interested in generating internal reflections, we set the coupling term to zero; thus the equation can now be easily factorized into the one-way form:

$$\left(\frac{1}{c(\underline{x})}\partial_t \pm \boldsymbol{\sigma}.\nabla\right)\mathbf{p} = 0. \tag{B-9}$$

Equation B-9 can also be written in its second-order form as

$$\left(\frac{1}{c^2(\underline{x})}\partial_t^2 - \nabla^2\right)\mathbf{p} = \pm\frac{\boldsymbol{\sigma}.\nabla c(\underline{x})}{c(\underline{x})}\boldsymbol{\sigma}.\nabla\mathbf{p}. \tag{B-10}$$

This equation has the same structure as equation B-1, except for the right-side term. This term attenuates velocity contrast-related reflections. This property is favorable in an RTM setting in which these reflections cause low-frequency artifacts in the formed image.

Equation B-10 is equivalent to equations B-9 and B-8 (with the reflection term set to zero) but due to its second-order nature and similarity with the conventional wave equation, it is numerically favorable in terms of finite-difference behavior.

Equation B-4 shows that Pauli matrices correspond to unit vectors in the three spatial dimensions, i.e., these matrices act as the vector basis that defines space. In analogy to quantum mechanical expectation operators (Wachter and Hoeber, 2006), we propose that the wavefield propagation direction can be calculated by forming inner products using these matrices

$$u_x = \frac{\mathbf{p}^H\boldsymbol{\sigma}_x\mathbf{p}}{\mathbf{p}^H\mathbf{p}}, \quad u_y = \frac{\mathbf{p}^H\boldsymbol{\sigma}_y\mathbf{p}}{\mathbf{p}^H\mathbf{p}}, \quad u_z = \frac{\mathbf{p}^H\boldsymbol{\sigma}_z\mathbf{p}}{\mathbf{p}^H\mathbf{p}}, \tag{B-11}$$

where u_x, u_y, and u_z are the propagation directions of the wavefield. These equations may then be used in an RTM 3D angle-gather generation setting in which the relationship is applied to source and receiver wavefields, or to determine the orientation of the estimated shifts in the proposed warping scheme in which the relationship is applied to the image wavefield.

APPENDIX C

EIGENVECTORS OF THE DIRAC OPERATOR

The eigenvalues and vectors of the Dirac operator can be computed by operating in the wavenumber domain; this is similar to the approach followed by Hokstad and Mittet (1999) for their depth extrapolation scheme:

$$\boldsymbol{\sigma}.\nabla\mathbf{p} \equiv \begin{pmatrix} ik_z & ik_x + k_y \\ ik_x - k_y & -ik_z \end{pmatrix}\mathbf{p}. \tag{C-1}$$

The eigenvalues are given by

$$k = \pm i\sqrt{k_x^2 + k_y^2 + k_z^2}. \tag{C-2}$$

The eigenvectors for positive and negative eigenvalues, respectively, are given by

$$\boldsymbol{\Psi}_+ = \begin{pmatrix} 1 \\ \frac{ik_x - k_y}{ik_z + i|k|\mathrm{sgn}(k_z)} \end{pmatrix}, \qquad \boldsymbol{\Psi}_- = \begin{pmatrix} \frac{-ik_x - k_y}{ik_z + i|k|\mathrm{sgn}(k_z)} \\ 1 \end{pmatrix}. \tag{C-3}$$

The signum function sets the sign convention; i.e., the sign of propagation direction is defined by the sign of the depth wavenumber.

Projecting an observed image wavefield onto the eigenvectors is defined by the relation

$$\mathbf{p}(\underline{x}) = \mathbf{K}[p] \equiv \int d\underline{k} e^{-i\underline{k}.\underline{x}} \frac{1}{\|\boldsymbol{\Psi}_\pm\|} \boldsymbol{\Psi}_\pm(\underline{k}) \times p(\underline{k}). \tag{C-4}$$

Both eigenvectors can be used in equation C-4. The sign of the resulting time shift depends on the choice.

REFERENCES

Baek, H., R. Burnstad, and T. Keho, 2014, Time/amplitude warping based on multiscale optimization: 84th Annual International Meeting, SEG, Expanded Abstracts, 4868–4872.

Baysal, E., D. D. Kosloff, and J. W. C. Sherwood, 1983, Reverse-time migration: Geophysics, **48**, 1514–1524, doi: 10.1190/1.1441434.

Bunks, C., F. M. Saleck, S. Zaleski, and G. Chavent, 1995, Multiscale seismic waveform inversion: Geophysics, **60**, 1457–1473, doi: 10.1190/1.1443880.

Dirac, P. A. M., 1928, The quantum theory of the electron: Proceedings of the Royal Society of London: Series A, **117**, 610–624, doi: 10.1098/rspa.1928.0023.

Gray, S. H., and W. P. May, 1994, Kirchhoff migration using eikonal equation traveltimes: Geophysics, **59**, 810–817, doi: 10.1190/1.1443639.

Gulunay, N., F. Gamar, H. Hoeber, M. Dyce, C. MacKenzie, and D. Whitcombe, 2007, Robust residual gather flattening: 77th Annual International Meeting, SEG, Expanded Abstracts, 229–233.

Hale, D., 2009, A method for estimating apparent displacement vectors from time-lapse seismic images: Geophysics, **74**, no. 5, V99–V107, doi: 10.1190/1.3184015.

Hale, D., 2013, Dynamic warping of seismic images: Geophysics, **78**, no. 2, S105–S115, doi: 10.1190/geo2012-0327.1.

Hall, S., 2006, A methodology for 7D warping and deformation monitoring using time-lapse seismic data: Geophysics, **71**, no. 4, O21–O31, doi: 10.1190/1.2212227.

Hill, N. R., 2001, Prestack Gaussian-beam depth migration: Geophysics, **66**, 1240–1250, doi: 10.1190/1.1487071.

Hokstad, K., and R. Mittet, 1999, Seismic depth migration with the Dirac equation: Geophysics, **64**, 925–933, doi: 10.1190/1.1444600.

Hubral, P., M. Tygel, and J. Schleicher, 1996, Seismic image waves: Geophysical Journal International, **125**, 431–442, doi: 10.1111/j.1365-246X.1996.tb00009.x.

McMechan, G. A., 1983, Migration by extrapolation of time-dependent boundary values: Geophysical Prospecting, **31**, 413–420, doi: 10.1111/j.1365-2478.1983.tb01060.x.

Mosher, C. C., T. H. Keho, A. A. Weglein, and D. J. Foster, 1996, The impact of migration on AVO: Geophysics, **61**, 1603–1615, doi: 10.1190/1.1444079.

Robertsson, J. O. A., J. O. Blanch, K. Nihei, and J. Tromp, 2012, Numerical modeling of seismic wave propagation: Gridded two-way wave-equation methods: SEG, Geophysics Reprint Series 28.

Sava, P., and S. Fomel, 2006, Time-shift imaging condition in seismic migration: Geophysics, **71**, no. 6, S209–S217, doi: 10.1190/1.2338824.

Schneider, W., 1978, Integral formulation for migration in two and three dimensions: Geophysics, **43**, 49–76, doi: 10.1190/1.1440828.

Thore, P., C. C. de Verdiere, and E. McManus, 2012, Estimation of 4D signal in complex media: A fast track approach: 82nd Annual International Meeting, SEG, Expanded Abstracts, doi: 10.1190/segam2012-0149.1.

Wachter, A., and H. Hoeber, 2006, Compendium of theoretical physics: Springer.

Whitmore, D., 1983, Iterative depth migration by backward time propagation: 53rd Annual International Meeting, SEG, Expanded Abstracts, 382–385.

Williamson, P. R., A. J. Cherrett, and P. A. Sexton, 2007, A new approach to warping for quantitative time — Lapse characterization: 69th Annual International Conference and Exhibition, EAGE, Extended Abstracts, P064.

Wu, R. S., and M. N. Toksoz, 1987, Diffraction tomography and multisource holography applied to seismic imaging: Geophysics, **52**, 11–25, doi: 10.1190/1.1442237.

Zhang, Y., and J. Sun, 2009, Practical issues in reverse time migration: True amplitude gathers, noise removal and harmonic source encoding: First Break, **27**, 53–59, doi: 10.3997/1365-2397.2009002.